Vacuum 232 (2025) 113893

Contents lists available at ScienceDirect

Vacuum

journal homepage: www.elsevier.com/locate/vacuum

Synthesis and irradiation behavior of $(Gd_{0.2}Sm_{0.2}Dy_{0.2}Er_{0.2}Yb_{0.2})_2Ti_2O_7$ high-entropy pyrochlore waste forms consolidated by spark plasma sintering

Xiaoyu Ji [a], Penghui Lei [a,*], Jiahao Chen [a], Jie Qiu [a,**], Qing Peng [b,c,d], Di Yun [a]

[a] School of Nuclear Science and Technology, Xi'an Jiaotong University, Xi'an, 710049, China
[b] State Key Laboratory of Nonlinear Mechanics, Institute of Mechanics, Chinese Academy of Sciences, Beijing, 100190, China
[c] Center of Materials Science and Optoelectronics Engineering, University of Chinese Academy of Sciences, Beijing, 100049, China
[d] Guangdong Aerospace Research Academy, Guangzhou, 511458, China

ARTICLE INFO

Handling Editor: Prof. L.G. Hultman

Keywords:
Nuclear waste form
High-entropy pyrochlore
Immobilization
Ion irradiation
Gas bubbles

ABSTRACT

The development of spent fuel reprocessing, which generates large amounts of high-level waste, necessitates effective management of waste containing radioactive elements. Pyrochlore ($A_2B_2O_7$) is considered one of the most promising immobilized matrixes for high-level waste due to its excellent physicochemical stability and irradiation resistance. A novel kind of high-entropy pyrochlore ceramic $(Gd_{0.2}Sm_{0.2}Dy_{0.2}Er_{0.2}Yb_{0.2})_2Ti_2O_7$, as an improved waste form matrix, was successfully synthesized using spark plasma sintering in this work. The mechanical properties, physical density, and microstructure of the densified pellets have been investigated in relation to different sintering temperatures (ranging from 1000 °C to 1400 °C). A single-component pyrochlore phase high-entropy ceramic was densified at 1300 °C, achieving a maximum hardness of 12.68 GPa and a density of 97.64 %. The irradiation tolerance of high-entropy pyrochlore was assessed by ion irradiation of 400 keV He^+ with 10×10^{17} ions/cm^2 at room temperature (RT). Ion irradiation can induce the transformation of the pyrochlore superlattice of $(Gd_{0.2}Sm_{0.2}Dy_{0.2}Er_{0.2}Yb_{0.2})_2Ti_2O_7$ into a fluorite sublattice. Compared to $Gd_2Ti_2O_7$, $(Gd_{0.2}Sm_{0.2}Dy_{0.2}Er_{0.2}Yb_{0.2})_2Ti_2O_7$ exhibits significantly reduced irradiation damage with suppressed generation and coalescence of helium bubbles due to chemical disorder and lattice distortion. High-entropy pyrochlore $(Gd_{0.2}Sm_{0.2}Dy_{0.2}Er_{0.2}Yb_{0.2})_2Ti_2O_7$ exhibits superior mechanical properties and irradiation resistance, suggesting its application as a promising immobilization matrix for nuclear waste.

1. Introduction

High-level waste (HLW) constitutes approximately 95 % of the total radioactivity of all radioactive waste. It contains minor actinides (such as ^{237}Np, ^{241}Am, ^{242}Cm) and some fission products (including ^{90}Sr, ^{60}Co, ^{137}Cs), which are highly toxicity, highly radioactive, and have long half-lives [1]. The safe disposal of HLW, ensuring maximum isolation from the biosphere, is essential for the continued development of nuclear energy [2]. At present, the most common approach for managing HLW worldwide is to first capture radioactive elements and confine them within durable waste forms, followed by deep geological disposal of the solidified HLW [3–5]. The immobilization matrix of HLW must satisfy several key requirements, including large waste-loading capacity, excellent mechanical properties, strong leaching resistance, high thermal stability, excellent irradiation resistance and technical feasibility [6,7]. Borosilicate glass systems have been widely used as the immobilization matrix of HLW globally, however, in practical engineering applications, several challenges remain, including component design, melting processing, and long-term stability evaluation of the solidified glass [8–10]. Therefore, identifying novel HLW immobilization materials with improved structural stability and irradiation resistance is of critical importance.

Artificial rock (synroc) is regarded as the second generation of HLW immobilization matrix, capable of incorporating radionuclides into its crystal lattice [11–13]. Among the various materials, pyrochlore is considered to be a very potential HLW immobilization matrix because of its outstanding qualities, including superior physical and chemical stability, excellent nuclide confinement, and remarkable irradiation

* Corresponding author.
** Corresponding author.
E-mail addresses: penghuilei@xjtu.edu.cn (P. Lei), qiu2021@xjtu.edu.cn (J. Qiu).

https://doi.org/10.1016/j.vacuum.2024.113893
Received 27 October 2024; Received in revised form 18 November 2024; Accepted 26 November 2024
Available online 28 November 2024

resistance [14–18]. The chemical structure of pyrochlore is $A_2B_2O_7$ (Fd-3m, lattice constant a = 0.9–1.2 nm), which is a defective fluorite structure (AX_2) featuring two cationic potentials and 1/8 anionic vacancies [19]. The A and B cations in $A_2B_2O_7$ pyrochlore can be occupied by lanthanides, transition metals, and actinides, indicating that $A_2B_2O_7$ pyrochlore has versatile radionuclide loading capacity [20,21]. However, HLW contains a wide variety of nuclides, and using single-component $A_2B_2O_7$ pyrochlore for the immobilization is generally limited to accommodating only one or two types of nuclides [22]. Solid solutions containing five or more cationic sublattices, stabilized by high configurational entropy, are referred to as high-entropy ceramics (HECs) [23]. In this way, high-entropy pyrochlores can incorporate multiple radionuclides at both the A-site and B-site cation positions. HECs exhibit four key high-entropy effects: the lattice distortion effect in crystallography, the kinetic sluggish diffusion effect, the thermodynamics effect, and the "cocktail" effect in performance, which collectively contribute to their superior performance compared to traditional ceramic materials [24]. As a result, HECs typically have superior properties compared to single-component conventional ceramic materials, including excellent phase stability [25–27], enhanced mechanical properties [24,28], improved corrosion resistance [29], and better irradiation resistance [30,31]. Numerous studies have indicated high-entropy pyrochlore could be a promising nuclear waste form [32–34]. However, to date, only a limited number of reports investigating the irradiation resistance of high-entropy pyrochlore. Furthermore, the microstructure evolution of high-entropy pyrochlore under irradiation is not yet fully understood.

In this work, a novel kind of high-entropy pyrochlore ceramic $(Gd_{0.2}Sm_{0.2}Dy_{0.2}Er_{0.2}Yb_{0.2})_2Ti_2O_7$ was successfully synthesized by spark plasma sintering (SPS), which is used to fabricate nuclear materials [35–40]. A Vickers hardness tester, scanning electron microscopy (SEM) and X-ray diffraction (XRD) were used to study the Vickers hardness, microstructure, density and phase constitution of high-entropy pyrochlore. And transmission electron microscopy (TEM) was employed to investigate the microstructure evolution of high-entropy pyrochlore $(Gd_{0.2}Sm_{0.2}Dy_{0.2}Er_{0.2}Yb_{0.2})_2Ti_2O_7$ and single-component pyrochlore $Gd_2Ti_2O_7$ irradiated at RT with 400 keV He^+ at a fluence of 1.0×10^{17} ions/cm^2. The effects of the components of pyrochlore on irradiation resistance have been investigated and revealed.

2. Material and experimental methods

2.1. Synthesis of high-entropy pyrochlore

High-entropy pyrochlore ceramic with chemical formula $(Gd_{0.2}Sm_{0.2}Dy_{0.2}Er_{0.2}Yb_{0.2})_2Ti_2O_7$ was synthesized by solid-state reaction, involving high energy ball milling (HEBM) and SPS under a vacuum of less than 2Pa. Gd_2O_3, Sm_2O_3, Dy_2O_3, Er_2O_3, Yb_2O_3, and TiO_2 (all with 99.99 % purity) were used as precursor materials and loaded into a milling tank inside a glove box under an argon atmosphere, with oxygen and water vapor levels maintained below 0.01 ppm. Stoichiometric precursor powders of 10 g, combined with 100 g WC balls, were homogenized in a HEBM system at 500 rpm for 10 h (15 min on and 5 min off each cycle). The homogenized powders were loaded into a 10 mm inner diameter graphite die and subsequently sintered using SPS. The consolidation of SPS sintering was carried out at various temperatures from 1100 °C to 1400 °C, with the process monitored by a pyrometer. A heating rate of 100 °C/min and a maximum sintering pressure of 50 MPa were applied for all sintering processes. The dwell time at the peak temperature and maximum pressure was 6 min. For comparison, $Gd_2Ti_2O_7$ was prepared using the same process. At RT, the density of the sintered pellets is measured using a density profiler with deionized water.

2.2. Irradiation experiments

The as-sintered $(Gd_{0.2}Sm_{0.2}Dy_{0.2}Er_{0.2}Yb_{0.2})_2Ti_2O_7$ and $Gd_2Ti_2O_7$ pellets were ground using SiC sandpapers from 400 grid to 5000 grid, and polished with diamond suspensions ranging from 3 μm to 1 μm. The polished samples, exhibiting a pyrochlore phase, were irradiated at RT by 400 keV He^+ ions with a fluence of 1.0×10^{17} ions/cm^2 using a NEC 400 kV ion implanter under a vacuum of 5×10^{-7}Pa at Xiamen University. The Stop and Range of Ions in Matter (SRIM) 2013 software with the quick Kinchin-Pease model was used to calculate the depth distribution and irradiation damage of injected He^+ ions. The atomic displacement threshold energies (E_d) for Gd, Sm, Dy, Er, Yb, and Ti elements were set to 35 eV, 27 eV, 34 eV, 37 eV, 27 eV and 30 eV, respectively [41]. Fig. 1 shows the implanted He^+ ion concentration and displacement damage distribution of $Gd_2Ti_2O_7$ and $(Gd_{0.2}Sm_{0.2}Dy_{0.2}Er_{0.2}Yb_{0.2})_2Ti_2O_7$ irradiated by 400 keV He^+ at a fluence of 1.0×10^{17} ions/cm^2, as calculated by SRIM. The peak He concentration of $Gd_2Ti_2O_7$ and $(Gd_{0.2}Sm_{0.2}Dy_{0.2}Er_{0.2}Yb_{0.2})_2Ti_2O_7$ reaches approximately 4.44 % and 4.20 % at a depth of 1.08 μm, respectively.

2.3. Characterization methods

The phase compositions were characterized by XRD (Bruker D8 ADVANCE, Germany). The theoretical density of the high-entropy pyrochlore samples was calculated using the precise lattice parameters of the pellets derived from the XRD data. $A_2B_2O_7$ high-entropy pyrochlore ceramics have a face-centered cubic structure, with each unit cell containing 8 $A_2B_2O_7$ formula units. The following formula is used to calculate the theoretical density:

$$d = \frac{m}{V} = \frac{8 \times M}{N_A \times V} = \frac{8 \times M}{N_A \times a^3} \quad (1)$$

where d is the theoretical density of the sample , M is the relative molecular mass of the sample, N_A is Avogadro's constant and a is the lattice constant of the sample.

A field emission SEM (Gemini SEM 500, Germany) under a vacuum of 5×10^{-5}Pa was performed to investigate the microstructure of the samples. The Vickers hardness of high-entropy pyrochlore was measured by a Vickers hardness tester. A 136° diamond indentation was generated on the surface of high-entropy pyrochlore samples with an applied load of 1.0 kg and maintained at room temperature for 10 s. The Vickers hardness (GPa) of the sample was calculated from formula (2):

$$H = 1854.4 \frac{P}{\alpha^2} \quad (2)$$

where H is the Vickers hardness of the samples, α is the average of the diagonal lengths of the two indentations, and P is the applied load.

The Thermo Scientific Helios 5 UX under a vacuum of less than 4.9×10^{-5}Pa was utilized to prepare cross-sectional TEM samples of the irradiated pellets using focused ion beam (FIB) techniques. The microstructure evolution and elemental distribution of the irradiated samples were characterized by TEM (Talos F200X, United States) and scanning TEM (STEM) with energy dispersive spectroscope (EDS) under a vacuum of 1.1×10^{-7}Pa.

3. Results and discussion

3.1. Characterization and mechanical properties of the sintered samples

$A_2B_2O_7$ oxides can exhibit three distinct crystal structures, including the monoclinic layered perovskite phase (M), the disordered fluorite structure (F), and the ordered pyrochlore structure (P). The crystal structure of $A_2B_2O_7$ oxide is mainly affected by the radius ratio ($\gamma = r_A/r_B$). When γ is less than 1.46, the oxide tends to form a F structure. When γ falls within in the range of 1.46–1.78, it is easy to form a P structure. When γ exceeds 1.78, it tends to form a M structure [42]. The pyrochlore structures of $Gd_2Ti_2O_7$ (γ = 1.7405) and $(Gd_{0.2}Sm_{0.2}Dy_{0.2}Er_{0.2}Yb_{0.2})_2Ti_2O_7$ (γ = 1.7200) are predicted by the radius ratio rule, as

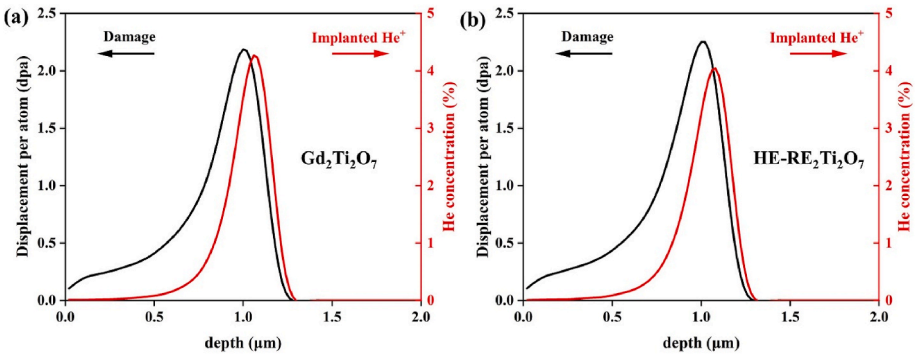

Fig. 1. The displacement damage and ion concentration distribution for (a) $Gd_2Ti_2O_7$ and (b) $(Gd_{0.2}Sm_{0.2}Dy_{0.2}Er_{0.2}Yb_{0.2})_2Ti_2O_7$ irradiated by 400 keV He^+ at a fluence of 1.0×10^{17} ions/cm^2 by SRIM.

indicated in Table 1 [43].

The XRD patterns of $Gd_2Ti_2O_7$ and $(Gd_{0.2}Sm_{0.2}Dy_{0.2}Er_{0.2}Yb_{0.2})_2Ti_2O_7$ high-entropy pyrochlore sintered by SPS at various temperatures were shown in Fig. 2. It can be observed that the high-entropy pyrochlores prepared at different sintering temperatures exhibit the typical diffraction peaks of the pyrochlore structure, confirming that the samples possess pyrochlore structure [44]. However, besides the pyrochlore's diffraction peaks, the high-entropy pyrochlores synthesized by SPS sintering at 1100 °C, 1200 °C and 1400 °C contain TiO_2 rutile phases and Yb_3O_4 phases, respectively. At a sintering temperature of 1300 °C, the diffraction peaks of the high-entropy pyrochlore closely match those of the $Gd_2Ti_2O_7$, with no additional phases detected. This indicates that the high-entropy pyrochlore sintered at 1300 °C using SPS has fully completed the solid-phase reaction, resulting in the formation of a face-centered cubic single-phase pyrochlore structure. $Gd_2Ti_2O_7$ samples confirmed by XRD analysis (Fig. 2) were sintered at 1300 °C using SPS.

Compared to the characteristic diffraction peaks of $Gd_2Ti_2O_7$ pyrochlore, the XRD diffraction peaks of high-entropy pyrochlore shifts approximately 0.13° toward a higher angle. This indicates that the lattice constant of the high-entropy pyrochlore decreases, leading to an increase in its theoretical density according to Bragg's Law [45]. According to calculations, the lattice constants of $Gd_2Ti_2O_7$ and $(Gd_{0.2}Sm_{0.2}Dy_{0.2}Er_{0.2}Yb_{0.2})_2Ti_2O_7$ are 10.1612 Å and 10.1174 Å, respectively. The theoretical densities of $Gd_2Ti_2O_7$ and $(Gd_{0.2}Sm_{0.2}Dy_{0.2}Er_{0.2}Yb_{0.2})_2Ti_2O_7$ were calculated to be 6.6135 g/cm^3 and 6.8229 g/cm^3, respectively (Table 1).

Fig. 3 shows the fractured surfaces of $Gd_2Ti_2O_7$ sintered at 1300 °C and $(Gd_{0.2}Sm_{0.2}Dy_{0.2}Er_{0.2}Yb_{0.2})_2Ti_2O_7$ sintered at temperatures from 1100 °C to 1400 °C, along with the density and Vickers hardness of $(Gd_{0.2}Sm_{0.2}Dy_{0.2}Er_{0.2}Yb_{0.2})_2Ti_2O_7$. In Fig. 3(a), Large numbers of open pores are observed in the sample of $(Gd_{0.2}Sm_{0.2}Dy_{0.2}Er_{0.2}Yb_{0.2})_2Ti_2O_7$ sintered at 1100 °C. These open holes could inhibit grain boundary migration, thereby slowing down grain growth [46]. It exhibits a Vickers hardness of 9.03 GPa, an average grain size of 139 ± 31 nm, and a density of 89.40 %. Similar microstructure morphologies are observed in Fig. 3(b) from the pellet sintered at 1200 °C. It exhibits, The Vickers hardness is 11.41 GPa, with a density of 94.57 %, and an average grain size of 429 ± 283 nm. As shown in Fig. 3(c), a slight grain growth in the sample is observed sintered at 1300 °C, with the Vickers hardness reaching a peak of 12.68 GPa. The density is 97.64 %, with an average grain size of 564 ± 170 nm. The $(Gd_{0.2}Sm_{0.2}Dy_{0.2}Er_{0.2}Yb_{0.2})_2Ti_2O_7$ pellet exhibits higher hardness and density compared to $Gd_2Ti_2O_7$ sintered at 1300 °C. This improvement attributed to the incorporation of multiple elements into the pyrochlore lattice, resulting in the formation of a pure-phase pyrochlore structure. Upon the temperature further to 1400 °C, the average grain size grows to 1.39 ± 0.47 μm, with a Vickers hardness of 12.45 GPa and a theoretical density of 97.87 %, as shown in Fig. 3(d). The cross-sectional surface exhibits a combination of trans-granular (indicated by red circle) and inter-granular (indicated by blue circle) fracture mechanisms. As displayed in Fig. 3(e), the density of $Gd_2Ti_2O_7$ sintered at 1300 °C is 97.07 % with an average grain size of 628 ± 271 nm and a Vickers hardness of 12.21 GPa.

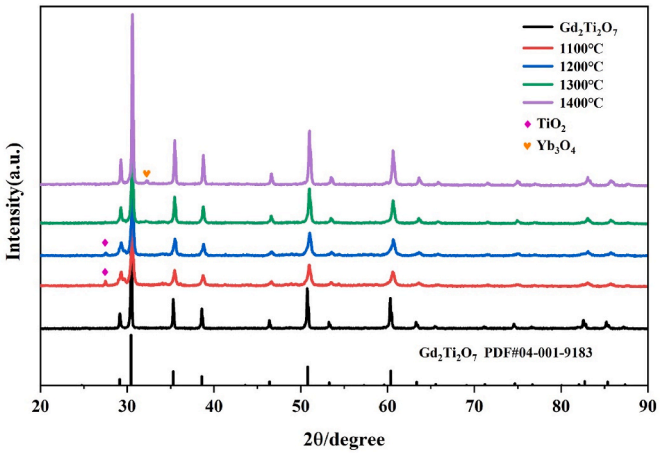

Fig. 2. XRD patterns of $Gd_2Ti_2O_7$ sintered at 1300 °C and $(Gd_{0.2}Sm_{0.2}Dy_{0.2}Er_{0.2}Yb_{0.2})_2Ti_2O_7$ sintered at 1100–1400 °C.

Table 1
Summary of the parameters of $Gd_2Ti_2O_7$ and $(Gd_{0.2}Sm_{0.2}Dy_{0.2}Er_{0.2}Yb_{0.2})_2Ti_2O_7$.

Compounds	r_A/r_B	Lattice Constants (Å)	Density (g/cm^3)
$Gd_2Ti_2O_7$	1.7405	10.1612	6.6135
$(Gd_{0.2}Sm_{0.2}Dy_{0.2}Er_{0.2}Yb_{0.2})_2Ti_2O_7$	1.7200	10.1174	6.8229

The densities and grain sizes substantially influence mechanical properties of the sintered ceramic samples. It can be concluded that the density and grain size of $(Gd_{0.2}Sm_{0.2}Dy_{0.2}Er_{0.2}Yb_{0.2})_2Ti_2O_7$ pellets increase with rising sintering temperature. The measured hardness initially rises, reaching the maximum hardness value of 12.68 GPa, and subsequently decreases with increasing of grain size, as displayed in Fig. 3(f). This reduction in hardness can be attributed to phase decomposition, as evidenced by XRD (Fig. 2) in pellets sintered at 1400 °C, which negatively impacts mechanical integrity. Consequently, the reduced hardness of the sample sintered at 1400 °C is primarily attributed to the detrimental effects of the secondary phase formation.

3.2. Microstructure of irradiated samples

The microstructure of the pellets irradiated by 400 keV He^+ with a fluence of 1.0×10^{17} ions/cm^2 are displayed in STEM dark field images

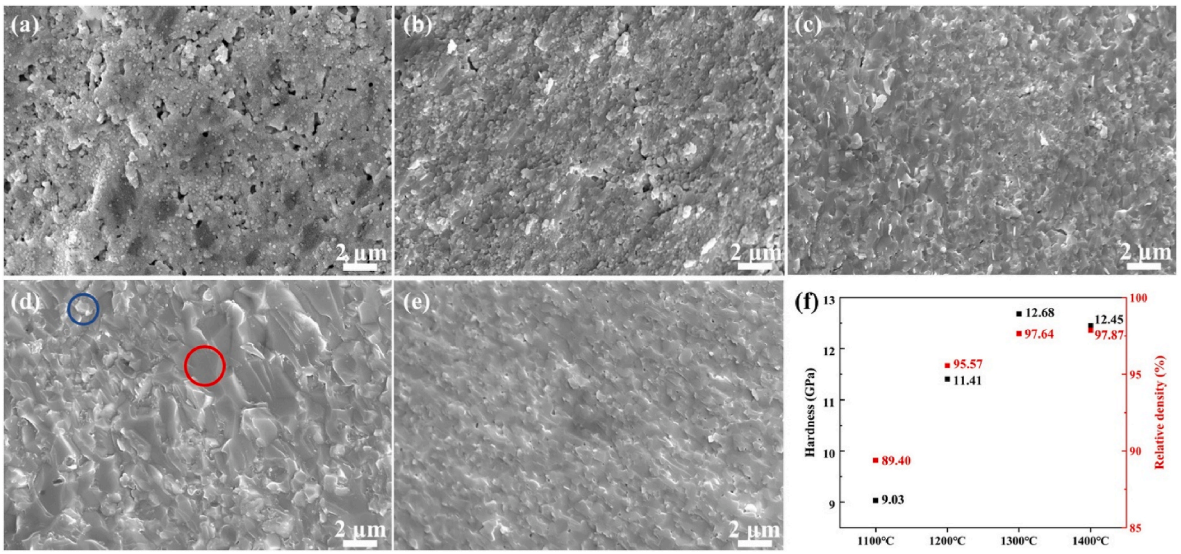

Fig. 3. (a) $(Gd_{0.2}Sm_{0.2}Dy_{0.2}Er_{0.2}Yb_{0.2})_2Ti_2O_7$ sintered at 1100 °C; (b) 1200 °C; (c) 1300 °C; (d) 1400 °C; (e) the cross-section fracture surfaces of $Gd_2Ti_2O_7$ sintered at 1300 °C; and (f) density and Vickers hardness of $(Gd_{0.2}Sm_{0.2}Dy_{0.2}Er_{0.2}Yb_{0.2})_2Ti_2O_7$.

in Fig. 4. The peak damage band and the incident depth of He ions in the $Gd_2Ti_2O_7$ sintered at 1300 °C, as illustrated in Fig. 4(a). The peak damage band is clearly visible, ranging from 0.90 μm to 1.21 μm in depth. It can be observed that the grain boundaries of $Gd_2Ti_2O_7$ in the peak irradiation damage region almost disappeared. The selected area electron diffraction (SAED) image from the region marked by the red circle shows a distinct amorphous ring along with diffraction spots, as shown in the inset image of Fig. 4(a). For the $(Gd_{0.2}Sm_{0.2}Dy_{0.2}Er_{0.2}Yb_{0.2})_2Ti_2O_7$ pellet sintered at 1300 °C, the microstructure morphology of the peak damage band is displayed in Fig. 4(b). It is clear that the grains of the irradiated area have not experienced significant amorphization, which is in line with the SAED image. Some diffraction spots from the region marked by the red circle in the high-entropy pyrochlore partially disappear, and amorphous rings begin to appear. This indicates that the degree of amorphization in the peak damage region is significantly higher for $Gd_2Ti_2O_7$ compared to $(Gd_{0.2}Sm_{0.2}Dy_{0.2}Er_{0.2}Yb_{0.2})_2Ti_2O_7$, indicating that $(Gd_{0.2}Sm_{0.2}Dy_{0.2}Er_{0.2}Yb_{0.2})_2Ti_2O_7$ exhibits superior irradiation resistance. Wang et al. reported that the E_d of each sublattice in high-entropy pyrochlore was higher than that of each sublattice in single-component pyrochlore $Gd_2Ti_2O_7$ through molecular dynamics simulations, which enhanced the irradiation resistance of high-entropy pyrochlore [47]. Similar results after irradiation have also been found in the high entropy carbide ceramics [48,49]. Moreover, the formation of anti-site defects at A-B sites enables high-entropy pyrochlore to exhibit excellent radiation defect recovery ability.

Fig. 5 shows the high-resolution TEM (HRTEM) image and SAED patterns of the grain A (from Fig. 4(a)) in $Gd_2Ti_2O_7$. The clear lattice structures along the [0 1 1] zone axis is presented by the atomic-resolution TEM image in Fig. 5(a). The measured d-spacings in the unirradiated region is 0.589 nm from the (1 1 1) crystal planes, which is in line with the PDF# 04-001-9183- $Gd_2Ti_2O_7$ (d = 0.587 nm). However, the measured d-spacings in the irradiated region is 0.309 nm, indicating irradiation induces a phase transformation from pyrochlore structure of $Gd_2Ti_2O_7$ to a fluorite sublattice. During the initial stages of ion irradiation, Wang et al. reported that the pyrochlore superlattice gradually become disordered and transformed into a fluorite sublattice, with the original interplanar spacing reducing by half [50]. Under the [0 1 1] zone axis, Fig. 5(b) shows an HRTEM image of the grain B (from Fig. 4 (b)) in $(Gd_{0.2}Sm_{0.2}Dy_{0.2}Er_{0.2}Yb_{0.2})_2Ti_2O_7$. The distance between the (111) crystal planes in the unirradiated region of $(Gd_{0.2}Sm_{0.2}Dy_{0.2}Er_{0.2}Yb_{0.2})_2Ti_2O_7$ is 0.603 nm, which is larger than the d-spacings in $Gd_2Ti_2O_7$. This increase is attributed to the lattice distortion effect of HECs. Similarly, the measured d-spacings in the irradiated region is 0.304 nm, indicating irradiation induces a phase

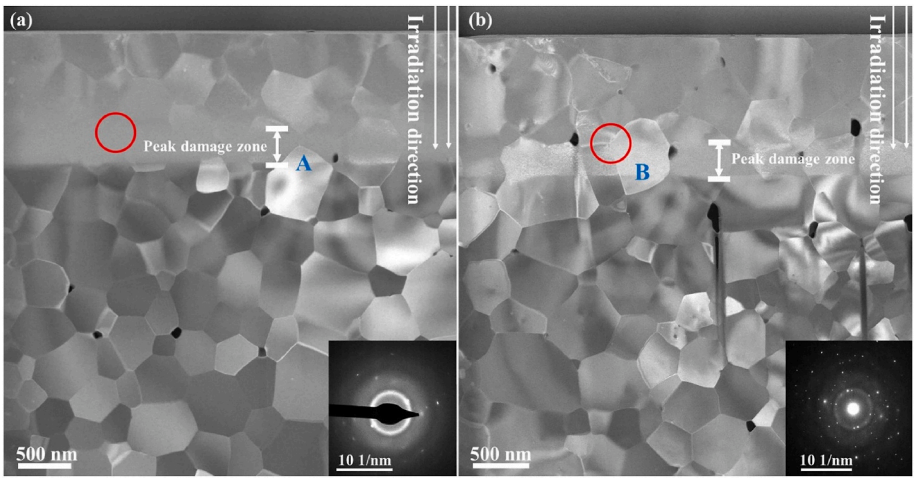

Fig. 4. STEM images and SAED patterns of (a) $Gd_2Ti_2O_7$ and (b) $(Gd_{0.2}Sm_{0.2}Dy_{0.2}Er_{0.2}Yb_{0.2})_2Ti_2O_7$ irradiated by 400 keV He^+ at a fluence of 1.0×10^{17} ions/cm^2.

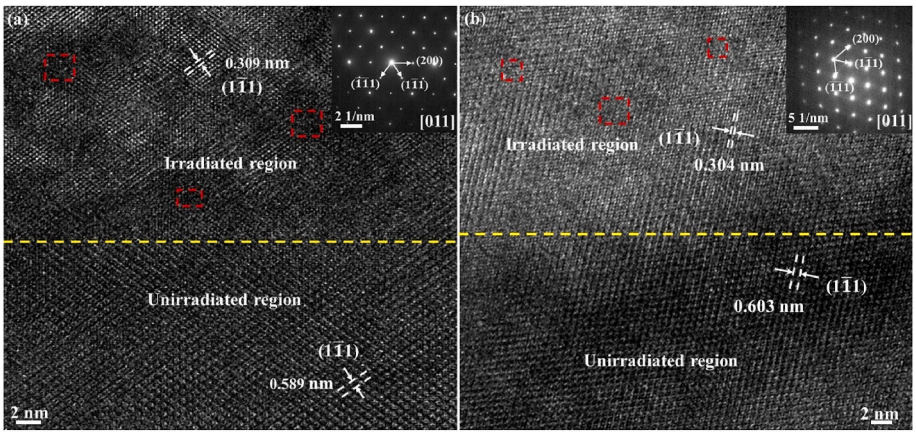

Fig. 5. HRTEM images and SAED patterns of (a)$Gd_2Ti_2O_7$ and (b)$(Gd_{0.2}Sm_{0.2}Dy_{0.2}Er_{0.2}Yb_{0.2})_2Ti_2O_7$.

transformation from pyrochlore structure of $(Gd_{0.2}Sm_{0.2}Dy_{0.2}Er_{0.2}Yb_{0.2})_2Ti_2O_7$ to a fluorite sublattice. In Fig. 5, irradiation-induced defects are highlighted by the red dashed boxes, which indicate areas of amorphization or atomic column misalignment.

3.3. Element distribution and gas bubbles behavior

The STEM images and EDS mapping of $Gd_2Ti_2O_7$ and $(Gd_{0.2}Sm_{0.2}Dy_{0.2}Er_{0.2}Yb_{0.2})_2Ti_2O_7$ are displayed in Fig. 6. The EDS results indicate that the elements in $Gd_2Ti_2O_7$ and $(Gd_{0.2}Sm_{0.2}Dy_{0.2}Er_{0.2}Yb_{0.2})_2Ti_2O_7$ are uniformly distributed in both irradiated and non-irradiated regions, with no evidence of element segregation. This suggests that all elements are well integrated into the crystal structure of pyrochlore, and irradiation does not induce segregation of elements in the samples. This indicates that the pyrochlore structure exhibits good phase stability.

The distribution of helium bubbles of the peak damage band in $Gd_2Ti_2O_7$ and $(Gd_{0.2}Sm_{0.2}Dy_{0.2}Er_{0.2}Yb_{0.2})_2Ti_2O_7$ samples after He^+ irradiation is investigated and shown in Fig. 7. The helium bubble sizes in $Gd_2Ti_2O_7$ and high-entropy pyrochlore samples are 2.30 nm and 2.23 nm, respectively. The number densities of helium bubbles are 1.86×10^{27} m^{-3} and 1.04×10^{27} m^{-3}, respectively. Compared to $Gd_2Ti_2O_7$, the size of the helium bubbles produced in high-entropy pyrochlore after He^+ irradiation is nearly the same, but the number density of helium bubbles is significantly reduced. This reduction could be attributed to the chemical disorder and lattice deformation induced by the presence of multiple rare earth elements, which significantly suppress the generation and coalescence of helium bubbles [51].

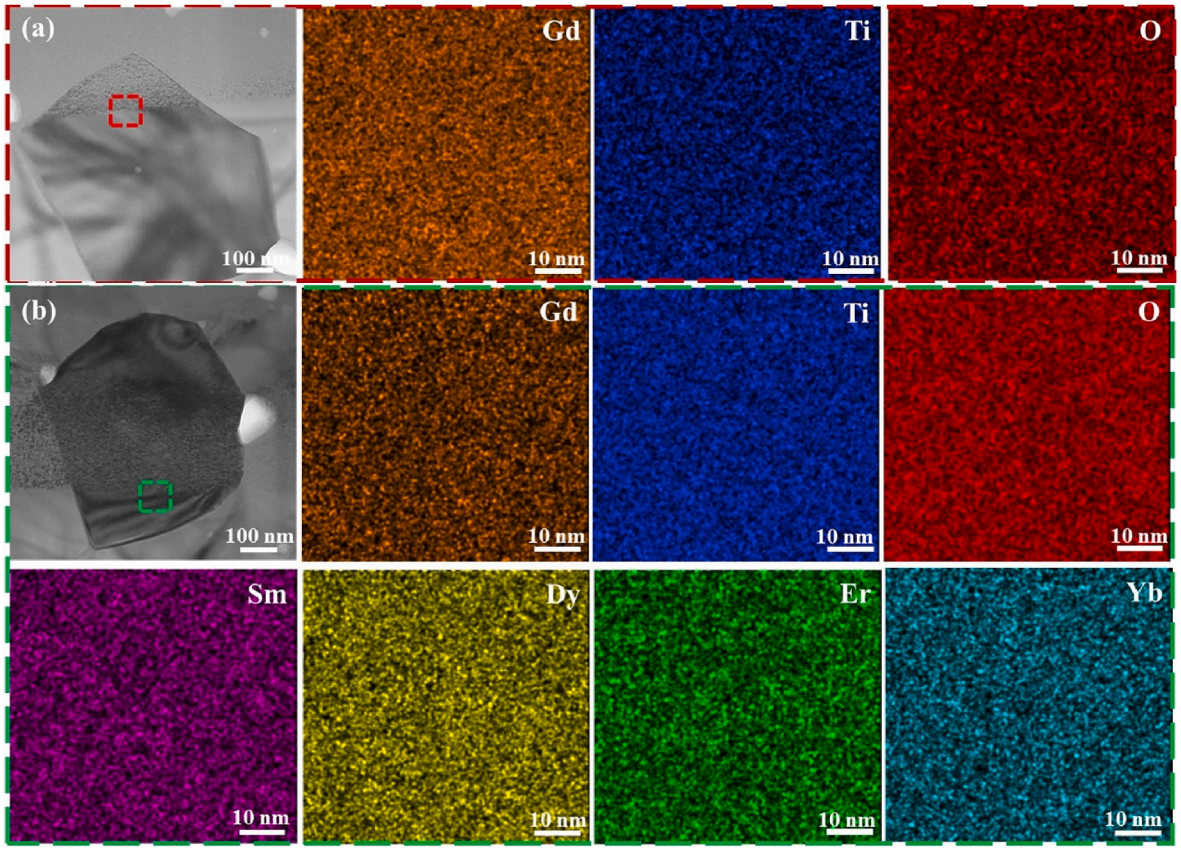

Fig. 6. STEM images and EDS mapping of (a)$Gd_2Ti_2O_7$ and (b)$(Gd_{0.2}Sm_{0.2}Dy_{0.2}Er_{0.2}Yb_{0.2})_2Ti_2O_7$ after 400 keV He^+ ions irradiation.

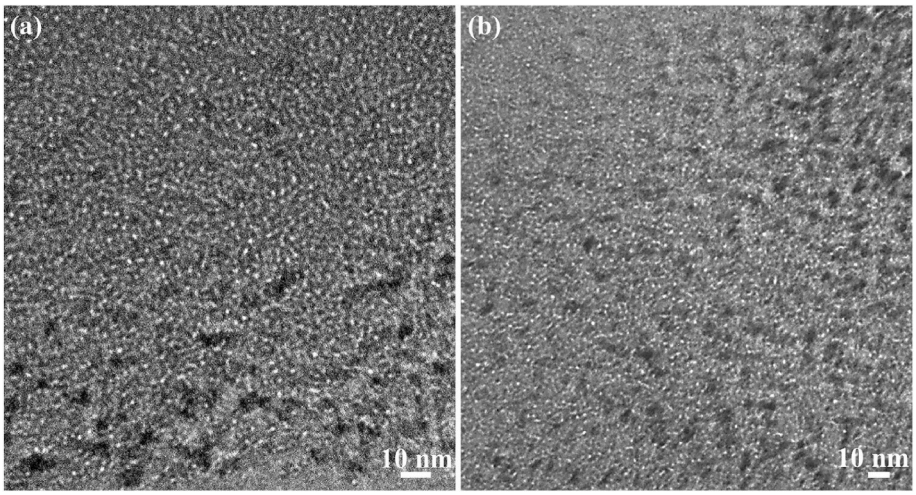

Fig. 7. The distribution of helium bubbles in (a) $Gd_2Ti_2O_7$ and (b) $(Gd_{0.2}Sm_{0.2}Dy_{0.2}Er_{0.2}Yb_{0.2})_2Ti_2O_7$ after 400 keV He^+ irradiation with a fluence of 1.0×10^{17} ions/cm^2.

4. Conclusion

A new type of $(Gd_{0.2}Sm_{0.2}Dy_{0.2}Er_{0.2}Yb_{0.2})_2Ti_2O_7$ high-entropy pyrochlore was prepared by SPS. According to XRD and SEM analysis, a single phase pyrochlore structure of high-entropy pyrochlore was formed at an SPS sintering temperature of 1300 °C, achieving a density of 97.64 % and a Vickers hardness of 12.68 GPa. Compared to the single-component pyrochlore $Gd_2Ti_2O_7$, high-entropy pyrochlore exhibits superior mechanical properties. Microstructure evolution of pyrochlore pellets irradiated at room temperature by 400 keV He^+ with a fluence of 1.0×10^{17} ions/cm^2 are studied. The degree of amorphization in the peak damage region is significantly lower for $(Gd_{0.2}Sm_{0.2}Dy_{0.2}Er_{0.2}Yb_{0.2})_2Ti_2O_7$, indicating that $(Gd_{0.2}Sm_{0.2}Dy_{0.2}Er_{0.2}Yb_{0.2})_2Ti_2O_7$ exhibits superior irradiation resistance. The distance between the (111) crystal planes in high-entropy pyrochlore is 0.371 nm, which is larger than the d-spacings in $Gd_2Ti_2O_7$. This increase is attributed to the lattice distortion effect of HECs. In the HRTEM images along the [0 1 1] zone axis, Irradiation-induced atomic column misalignment areas are visible. Ion irradiation can induce the transformation of the pyrochlore superlattice of $(Gd_{0.2}Sm_{0.2}Dy_{0.2}Er_{0.2}Yb_{0.2})_2Ti_2O_7$ into a fluorite sublattice. The high-entropy pyrochlore structure exhibits good phase stability after irradiation, with no evidence of element segregation. Compared to $Gd_2Ti_2O_7$, the helium bubble size in high-entropy pyrochlore after He^+ irradiation is similar, but the number density of helium bubbles significantly decreases, from 1.86×10^{27} m^{-3} at 2.30 nm to 1.04×10^{27} m^{-3} at 2.23 nm. The chemical disorder and lattice distortion in $(Gd_{0.2}Sm_{0.2}Dy_{0.2}Er_{0.2}Yb_{0.2})_2Ti_2O_7$ significantly suppress the generation and coalescence of helium bubbles. This study concludes that $(Gd_{0.2}Sm_{0.2}Dy_{0.2}Er_{0.2}Yb_{0.2})_2Ti_2O_7$ high-entropy pyrochlore exhibits excellent mechanical properties and radiation resistance, making it a promising candidate as an immobilizing matrix for high-level radioactive waste. The long-term evolution of microstructures and defects might be interested in a further study.

CRediT authorship contribution statement

Xiaoyu Ji: Writing – original draft, Methodology. **Penghui Lei:** Writing – review & editing, Investigation. **Jiahao Chen:** Data curation. **Jie Qiu:** Writing – review & editing. **Qing Peng:** Writing – review & editing. **Di Yun:** Methodology, Conceptualization.

Declaration of competing interest

We declare that we have no known competing financial interests or personal relationships that could have appeared to influence the work reported in this paper entitled "Synthesis and Irradiation Behavior of $(Gd_{0.2}Sm_{0.2}Dy_{0.2}Er_{0.2}Yb_{0.2})_2Ti_2O_7$ High-entropy Pyrochlore Waste Forms Consolidated by Spark Plasma Sintering".

Acknowledgements

This work is supported by the National Natural Science Foundation of China (12205232) and the Basic Scientific Research Fund of Xi'an Jiaotong University (xzy012022077). Q. P. would like to acknowledge the support from the Strategic Priority Research Program of the Chinese Academy of Sciences (Grant No. XDB0620103), the National Natural Science Foundation of China (Grant No. 12272378), and the High-level Innovation Research Institute Program of Guangdong Province (Grant No. 2020B0909010003). We thank Dr. Chao Li at Instrument Analysis Center of Xi'an Jiaotong University for his assistance with TEM and image analysis.

Data availability

The data that has been used is confidential.

References

[1] R.C. Ewing, Nuclear waste forms for actinides, Proc. Natl. Acad. Sci. U. S. A. 96 (7) (1999) 3432–3439.
[2] M.M. Abu-Khader, Recent advances in nuclear power: a review, Prog. Nucl. Energy 51 (2) (2009) 225–235.
[3] L. Wang, T. Liang, Ceramics for high level radioactive waste solidification, J. Adv. Ceramics 1 (3) (2012) 194–203.
[4] W.J. Weber, R.C. Ewing, Plutonium immobilization and radiation effects, Science 289 (5487) (2000) 2051–2052.
[5] M.-S. Yim, K. Linga Murty, Materials issues in nuclear-waste management, JOM 52 (9) (2000) 26–29.
[6] I.W. Donald, B.L. Metcalfe, R.N.J. Taylor, The immobilization of high level radioactive wastes using ceramics and glasses, J. Mater. Sci. 32 (22) (1997) 5851–5887.
[7] A. Gentils, L. Thomé, J. Jagielski, S. Enescu, F. Garrido, M. Beauvy, G. Blaise, High temperature behaviour of fission product analogues implanted into nuclear ceramics, Vacuum 70 (2–3) (2003) 123–129.
[8] W. Lutze, R.C. Ewing, Radioactive Waste Forms for the Future, 1988.
[9] P.K. Mishra, V. De, D.E. Ghongane, T.P. Valsala, M.S. Sonavane, Preparation and characterisation of glass product with modified composition for vitrification of high level radioactive waste, J. Therm. Anal. Calorim. 112 (1) (2013) 103–108.
[10] J.D. Vienna, Nuclear waste vitrification in the United States: recent developments and future options, Int. J. Appl. Glass Sci. 1 (3) (2010) 309–321.
[11] A.I. Orlova, M.I. Ojovan, Ceramic mineral waste-forms for nuclear waste immobilization, Materials 12 (16) (2019) 2638.
[12] A.E. Ringwood, S.E. Kesson, N.G. Ware, W. Hibberson, A. Major, Immobilisation of high level nuclear reactor wastes in SYNROC, Nature 278 (5701) (1979) 219–223.

[13] E.R. Vance, Synroc: a suitable waste form for actinides, MRS Bull. 19 (12) (1994) 28–32.
[14] S. Chen, X. Shu, L. Wang, F. Chi, D. Shao, Y. Ding, X. Yuan, Q. Qing, X. Lu, Effects of alpha irradiation on Nd2Zr2O7 matrix for nuclear waste forms, J. Australian Ceramic Sc. 54 (1) (2018) 33–38.
[15] J. Lian, L.M. Wang, R.G. Haire, K.B. Helean, R.C. Ewing, Ion beam irradiation in La2Zr2O7–Ce2Zr2O7 pyrochlore, Nuclear Instruments Methods Phys. Res. Section B-beam Interactions Mater. Atoms 218 (2004) 236–243.
[16] X. Lu, X. Shu, D. Shao, S. Chen, H. Zhang, X. Yuan, F. Chi, Radiation stability of Gd2Zr2O7 and Nd2Ce2O7 ceramics as nuclear waste forms, Ceram. Int. 44 (1) (2018) 760–765.
[17] S.X. Wang, B.D. Begg, L.M. Wang, R.C. Ewing, W.J. Weber, K.V.G. Kutty, Radiation stability of gadolinium zirconate: a waste form for plutonium disposition, J. Mater. Res. 14 (12) (1999) 4470–4473.
[18] S. Yamazaki, T. Yamashita, T. Matsui, T. Nagasaki, Thermal expansion and solubility limits of plutonium-doped lanthanum zirconates, J. Nucl. Mater. 294 (2001) 183–187.
[19] B.C. Chakoumakos, Systematics of the pyrochlore structure type, ideal A2B2X6Y, J. Solid State Chem. 53 (1) (1984) 120–129.
[20] M.A. Subramanian, G. Aravamudan, G.V. Subba Rao, Oxide pyrochlores — a review, Prog. Solid State Chem. 15 (2) (1983) 55–143.
[21] F. Luo, B. Yuan, M. Wen, Y. Miao, Y. Lu, J. Chen, X. Lu, G. Wei, F. Dong, Insight into the effect of Nd2O3 and CeO2 co-doped Gd2Zr2O7 ceramics without structural design: phase evolution and chemical durability, Vacuum 203 (2022) 111256.
[22] X. Shu, L. Fan, X. Lu, Y. Xie, Y. Ding, Structure and performance evolution of the system (Gd1−xNdx)2(Zr1−yCey)2O7 (0≤x, y≤1.0), J. Eur. Ceram. Soc. 35 (11) (2015) 3095–3102.
[23] C.M. Rost, E. Sachet, T. Borman, A. Moballegh, E.C. Dickey, D. Hou, J.L. Jones, S. Curtarolo, J.-P. Maria, Entropy-stabilized oxides, Nat. Commun. 6 (1) (2015) 8485.
[24] C. Oses, C. Toher, S. Curtarolo, High-entropy ceramics, Nat. Rev. Mater. 5 (4) (2020) 295–309.
[25] H. Chen, H. Xiang, F.-Z. Dai, J. Liu, Y. Lei, J. Zhang, Y. Zhou, High porosity and low thermal conductivity high entropy (Zr0.2Hf0.2Ti0.2Nb0.2Ta0.2)C, J. Mater. Sci. Technol. 35 (8) (2019) 1700–1705.
[26] Z. Weijun, Y. Fan, L. Zhaoli, C. Heng, S. Zhiheng, Z. Xuesong, W. Kaixian, X. Liyan, A novel (La0.2Sm0.2Eu0.2Gd0.2Tm0.2)2Zr2O7 high-entropy ceramic nanofiber with excellent thermal stability, Ceram. Int. 47 (20) (2021) 29379–29385.
[27] H. Xiang, Y. Xing, F.-z. Dai, H. Wang, L. Su, L. Miao, G. Zhang, Y. Wang, X. Qi, L. Yao, H. Wang, B. Zhao, J. Li, Y. Zhou, High-entropy ceramics: present status, challenges, and a look forward, J. Adv. Ceramics 10 (3) (2021) 385–441.
[28] E. Castle, T. Csanádi, S. Grasso, J. Dusza, M. Reece, Processing and properties of high-entropy ultra-high temperature carbides, Sci. Rep. 8 (1) (2018) 8609.
[29] L. Zhou, F. Li, J.-X. Liu, S.-K. Sun, Y. Liang, G.-J. Zhang, High-entropy A2B2O7-type oxide ceramics: a potential immobilising matrix for high-level radioactive waste, J. Hazard Mater. 415 (2021) 125596.
[30] Y. Li, Y. Lei, S. Zhao, H. Xiao, H. Liu, Y. Wang, Y. Luo, J. Zhang, J. Wang, R. C. Ewing, C. Wang, Phase transformation and radiation resistance of B-site high entropy pyrochlores, Scripta Mater. 229 (2023) 115367.
[31] L. Xu, M. Niu, H. Wang, L. Su, H. Gao, L. Zhuang, Response of structure and mechanical properties of high entropy pyrochlore to heavy ion irradiation, J. Eur. Ceram. Soc. 42 (14) (2022) 6624–6632.
[32] K. Yang, K. Bryce, W. Zhu, D. Zhao, J. Lian, Multicomponent pyrochlore solid solutions with uranium incorporation – a new perspective of materials design for nuclear applications, J. Eur. Ceram. Soc. 41 (4) (2021) 2870–2882.
[33] K. Yang, P. Lei, T. Yao, B. Gong, Y. Wang, M. Li, J. Wang, J. Lian, A systematic study of lanthanide titanates (A2Ti2O7) chemical durability: corrosion mechanisms and control parameters, Corrosion Sci. 185 (2021) 109394.
[34] K. Yang, K. Bryce, T. Yao, D. Zhao, J. Lian, Chemical durability and corrosion-induced microstructure evolution of compositionally complex titanate pyrochlore waste forms with uranium incorporation, J. Eur. Ceram. Soc. 44 (2) (2024) 1102–1114.
[35] P. Lei, X. Ji, J. Qiu, J. Si, T. Peng, C. Teng, L. Wu, The influence of grain size on microstructure evolution in CeO2 under xenon ion irradiation, Nanomaterials 14 (18) (2024) 1498.
[36] T. Yao, X. Guo, P. Lei, Y. Wang, G.S. Frankel, J. Lian, Corrosion interactions between stainless steel and lead vanado-iodoapatite nuclear waste form part II, npj Mater. Degrad. 4 (1) (2020) 15.
[37] F. Cappia, M. Cullison, T. Chen, B. Kombaiah, K. Bawane, F. Teng, J. Madden, E. Perez, T. Yao, P. Lei, Grain subdivision and structural modifications by high-energy heavy ions in UO2 with different initial grain size, Nucl. Instrum. Methods Phys. Res. Sect. B Beam Interact. Mater. Atoms 515 (2022) 48–60.
[38] X. Guo, S. Gin, P. Lei, T. Yao, H. Liu, D.K. Schreiber, D. Ngo, G. Viswanathan, T. Li, S.H. Kim, Reply to: how much does corrosion of nuclear waste matrices matter, Nat. Mater. 19 (9) (2020) 962–963.
[39] X. Guo, S. Gin, P. Lei, T. Yao, H. Liu, D.K. Schreiber, D. Ngo, G. Viswanathan, T. Li, S.H. Kim, Self-accelerated corrosion of nuclear waste forms at material interfaces, Nat. Mater. 19 (3) (2020) 310–316.
[40] P. Lei, N. Jiang, J. Hao, Q. Peng, P. Qi, F. Shi, Y. Hang, Q. Li, C. Ye, Effect of hydrogen ion irradiation on the mechanical properties of thermally aged Z3CN20. 09M duplex stainless steel, Vacuum (2024) 113757.
[41] A.Y. Konobeyev, U. Fischer, Y.A. Korovin, S.P. Simakov, Evaluation of effective threshold displacement energies and other data required for the calculation of advanced atomic displacement cross-sections, Nuclear Energy Tech. 3 (3) (2017) 169–175.
[42] R.C. Ewing, W.J. Weber, J. Lian, Nuclear waste disposal—pyrochlore (A2B2O7): nuclear waste form for the immobilization of plutonium and “minor” actinides, J. Appl. Phys. 95 (2004) 5949–5971.
[43] R. Shannon, Revised effective ionic radii and systematic studies of interatomic distances in halides and chalcogenides, Acta Crystallogr. 32 (1976) 751–767.
[44] K.E. Sickafus, L. Minervini, R.W. Grimes, J.A. Valdez, M. Ishimaru, F. Li, K. J. McClellan, T. Hartmann, Radiation tolerance of complex oxides, Science 289 (5480) (2000) 748–751.
[45] W.H. Bragg, The reflection of X-rays by crystals, Nature 91 (2280) (1913) 477, 477.
[46] P. Lei, K. Yang, T. Shi, M. Wei, G. Ran, C. Lu, Surface alteration and chemical durability of hollandite (Cr, Al and Ti) consolidated by spark plasma sintering in acid solution, J. Nucl. Mater. 568 (2022) 153892.
[47] Z. Wang, L. Zhou, C. Liu, Y. Li, The irradiation resistance and mechanical properties of the high-entropy zirconate pyrochlore (La0.2Nd0.2Sm0.2Eu0.2Gd0.2)2Zr2O7, Nuclear Inst. and Methods in Physics Research B 549 (2024) 165285.
[48] G. Zhang, N. Daghbouj, A. AlMotasem, Z. Fang, T. Wang, J. Zhang, T. Zhang, J. Li, J. Zhou, S. Xu, Exploring radiation damage in (Hf0. 2Zr0. 2Ta0. 2Ti0. 2Nb0. 2) C high-entropy carbide ceramic: integrating experimental and atomistic investigations, Int. J. Refract. Metals Hard Mater. (2024) 106755.
[49] J. Zhang, S. Xu, C. Wen, J. Huang, J. Li, Z. Wu, R. Wang, F. Ge, G. Zhang, Z. Fang, A study on He ion irradiation damage in (Ti0. 25Zr0. 25Nb0. 25Ta0. 25) C high-entropy carbide ceramics from room temperature to 700° C, J. Eur. Ceram. Soc. 45 (1) (2025) 116855.
[50] S. Wang, L. Wang, R. Ewing, G. Was, G. Lumpkin, Ion irradiation-induced phase transformation of pyrochlore and zirconolite, Nucl. Instrum. Methods Phys. Res. Sect. B Beam Interact. Mater. Atoms 148 (1–4) (1999) 704–709.
[51] F. Wang, X. Yan, L. Shao, M. Nastasi, B. Cui, Irradiation Damage Behavior in Novel High-Entropy Carbide Ceramics, 2019.